Journal of Alloys and Compounds 1051 (2026) 186051

Contents lists available at ScienceDirect

Journal of Alloys and Compounds

journal homepage: www.elsevier.com/locate/jalcom

Research article

Local structure and dynamics of a Zr-based bulk metallic glass during ex situ and in situ annealing

Olivia Vaerst [a], Harald Rösner [a,*], Martin Peterlechner [b], Gerhard Wilde [a]

[a] University of Münster, Institute of Materials Physics, Wilhelm-Klemm-Str. 10, Münster, 48149, Germany
[b] Karlsruhe Institute of Technology, Laboratory for Electron Microscopy, Engesserstr. 7, Karlsruhe, 76131, Germany

ARTICLE INFO

Keywords:
Bulk metallic glass
Structural relaxation
In situ transmission electron microscopy
Medium-range order
Atomic mobility

ABSTRACT

Advanced transmission electron microscopy (TEM) techniques are utilized to investigate the structural evolution and underlying mechanisms driving relaxation in metallic glasses. We quantify changes in medium-range order (MRO) using fluctuation electron microscopy (FEM), while electron correlation microscopy (ECM) combined with in situ heating allows us to directly probe local dynamics with unprecedented spatial resolution. FEM analysis provides a semi-quantitative estimate of the MRO volume fraction, based on either the peak height or the peak integral of the variance. This measure was found to increase in structurally relaxed samples compared to the as-cast condition, observed across both predefined annealed states and during *in situ* heating. Complementary *in situ* analyses uncover a temperature-dependent reduction in atomic mobility. This decrease in dynamics—which aligns with the phenomenon of irreversible structural relaxation, often termed "aging"—is examined with high spatial resolution for the first time. The findings on structural modifications and local relaxation behavior during heating are discussed in detail and compared with results obtained via other characterization methods and across different material systems, providing a comprehensive understanding of relaxation processes in metallic glasses.

1. Introduction

Bulk metallic glasses (BMGs) are alloys that predominantly exist in a thermodynamic non-equilibrium state, characterized by a lack of long-range order and the presence of short- to medium-range order (SRO and MRO). This non-equilibrium condition is established during vitrification from the equilibrium liquid state that enable the possibility of various dynamics processes to relax the glass toward a more stable state [1]. It is important to distinguish these relaxation processes occurring within the glassy state from the intrinsic relaxation dynamics present in the metastable equilibrium state above the glass transition temperature, known as the supercooled liquid region. The latter are typically quasi-reversible α-relaxation processes. In contrast, processes in the glassy state can be induced by thermal treatments below the glass transition temperature and are called structural relaxation or "aging". Structural relaxation lowers the excess enthalpy of the material [2–4]. With respect to the potential energy landscape, a structural relaxation process transfers the glass from a local basin with a higher excess free enthalpy to a lower one, changing the configurational state [5–7]. This process is highly complex and is often depicted through multi-dimensional illustrations [5,8].

Fig. 1 provides a straightforward schematic representation of structural relaxation phenomena as they relate to changes in enthalpy that occur during differential scanning calorimetry (DSC) experiments [9]. Structural relaxation also increases the heat capacity (bottom figure in Fig. 1), resulting in a more stable glass state. For sufficiently long annealing treatments that avoid crystallization at specific temperatures below the glass transition temperature, the glass can even attain a state similar to the metastable equilibrium state of the supercooled liquid. This effect is confirmed by heat capacity and viscosity measurements [10,11]. The current study focuses on the structural relaxation processes within the non-equilibrium glass state, namely, on structural and dynamics modifications during structural relaxation (i.e. during "aging").

Structural relaxation induced by thermal treatments, that is, annealing below the glass transition temperature, is not only accompanied by a reduction in excess free volume resulting in increased material density, but also associated with atomic rearrangements leading to irreversible structural changes [12]. All of this affects the properties of the glassy material [12–16]. The correlation between structure and properties is established and accepted in a continuum description based

* Corresponding author.
E-mail addresses: ovaerst@uni-muenster.de (O. Vaerst), rosner@uni-muenster.de (H. Rösner), martin.peterlechner@kit.edu (M. Peterlechner), gwilde@uni-muenster.de (G. Wilde).

https://doi.org/10.1016/j.jallcom.2026.186051
Received 14 October 2025; Received in revised form 17 December 2025; Accepted 6 January 2026
Available online 7 January 2026

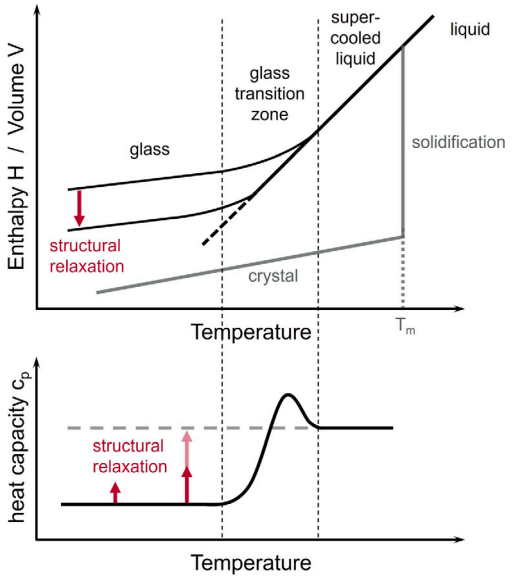

Fig. 1. Top: Enthalpy H and volume V as a function of temperature during the vitrification of a glass from the liquid state. The arrow indicates the enthalpy change connected with structural relaxation (or "aging") during isothermal annealing. Bottom: Heat capacity c_p during heating of a glass showing the glass transition as an endothermic signal. The red arrows show the time- and temperature-dependent effect of structural relaxation by isothermal annealing on the heat capacity. This sets the system into a more stable state, ultimately reaching a state corresponding to the supercooled liquid indicated by the brighter arrow pointing towards the dashed horizontal line resembling the supercooled liquid state.

on mass density. However, the specifics of the structural changes and mechanisms involved in such aging processes are not adequately understood at the particle level, even though numerous studies have employed X-ray diffraction (XRD) for structural analysis [4], fluctuation electron microscopy (FEM) to investigate the MRO of BMGs [17,18], and X-ray photon correlation spectroscopy (XPCS) to analyze dynamics [19,20].

In the present work, different enthalpic/configurational states of commercial BMG AMZ4 ($Zr_{59.3}Cu_{28.8}Al_{10.4}Nb_{1.5}$ at.%) are investigated using advanced methods within the context of transmission electron microscopy (TEM) to obtain detailed microstructural insights into structural relaxation processes. To achieve this, we analyze an as-cast sample in conjunction with a bulk annealed sample (heat treated without reaching a metastable state) and compare the results with those of a sample that was annealed *in situ* during the same investigations. Specifically, fluctuation electron microscopy is used to analyze the structure of the material in the three states: as-cast, annealed, and during *in situ* heating, allowing us to track variations in MRO induced by structural relaxation. Furthermore, electron correlation microscopy (ECM), which serves as the TEM equivalent of XPCS [21,22], is employed to examine the local dynamics in the two states (as-cast and annealed) at room temperature, as well as the dynamics changes occurring during *in situ* heating of the as-cast state. In contrast to XPCS, the use of ECM provides the first spatially resolved results that are directly correlated with local analyses of the medium-range order in the same specimens. This approach enables a comprehensive characterization of the changes in both structure and dynamics during the structural relaxation of a metallic glass. In particular, the observed changes in MRO with progressing structural relaxation are identified and confirmed employing *in situ* FEM. Furthermore, the dynamics extracted from the *in situ* ECM measurements shows a stable aging behavior of the material.

2. Materials and methods

2.1. Sample preparation

AMZ4 bulk material ($Zr_{59.3}Cu_{28.8}Al_{10.4}Nb_{1.5}$ at.%) was supplied by Amorphous Metal Solutions GmbH in the form of a cylindrical rod as-cast, measuring 3 mm in diameter and 6 mm in length. The amorphous state was verified using XRD (Siemens D5000) and DSC (Mettler Toledo DSC3), which displayed both the glass transition and crystallization temperatures (see Fig. 2), consistent with findings reported in the literature [23]. In addition to examining the as-cast material, we also investigated an annealed sample state of the glass. Annealing was performed on a piece of the as-cast rod by heating to a temperature of $T_{annealing}$ = 275°C (0.8 T_g) at a rate of 20 K/min using the DSC. The sample was held at this temperature for 4 h, followed by cooling to room temperature at a rate of 50 K/min.

TEM samples of the as-cast and annealed material were prepared using a focused ion beam (FIB) device (ZEISS Crossbeam 340). The lamellae were cut using Ga^+ ions with beam energies of 30 kV. The final polishing was performed with an ion beam of 5 kV and 10 pA. After being thinned to electron transparency, the lamellae intended for room temperature experiments were placed on copper grids, while those designated for heating experiments were transferred to a MEMS E-chip (Protochips Fusion Select). Detailed steps for this transfer process with the FIB device used are explained in [24]. The room temperature samples were plasma cleaned for 90 s prior to TEM measurements.

2.2. TEM measurements

All TEM measurements were performed at 300 kV in a Thermo Fisher Scientific FEI TITAN Themis G3 60–300 transmission electron microscope. A Protochips Fusion AX holder was used for the heating experiments. The basic characterizations of each sample and measurement position included thickness measurements conducted using the log-ratio method [25], which used the low-loss part of the electron energy loss spectrum (EELS) obtained with a Quantum 965 Gatan Imaging Filter. The relative thickness was determined based on the free mean path λ, which measures 78 nm for AMZ4. This calculation was performed using the script from D. Mitchell in *Digital Micrograph*™ [26,27].

2.3. Fluctuation electron microscopy, measurement parameters and data analysis

Fluctuation electron microscopy (FEM) is an electron diffraction technique used to investigate MRO in disordered material systems [28–30]. It is based on a statistical analysis of diffracted intensities in nanobeam diffraction patterns (NBDP) [31,32]. Such diffraction patterns are recorded in microdiffraction STEM mode by scanning parallel coherent nanometer-sized probes over a sample region [29,33]. The advantage of FEM is that it captures information about higher-order atomic correlations - specifically, pair–pair correlations involving three- and four-body correlations - and hence describes the structural motifs and MRO in disordered materials (cluster size and volume fraction) [28,29,31]. The diffracted intensities $I(\vec{k}, R, \vec{r})$, obtained from the position of the $\vec{r}$, show spatial variations that can be quantified by calculating the normalized variance

$$V(\vec{k}, R) = \frac{\left\langle I^2(\vec{k}, R, \vec{r})\right\rangle}{\left\langle I(\vec{k}, R, \vec{r})\right\rangle^2} - 1, \quad (1)$$

where $\langle ... \rangle$ denotes the averaging over different sample positions $\vec{r}$ or nanometer-sized volumes, and $\vec{k}$ is the scattering vector [34,35]. R is the spatial resolution given by the full width at half maximum (FWHM) of the electron probe. Acquiring NBDP with different probe sizes R is called variable resolution FEM (VR-FEM) [29,30,33,35,36].

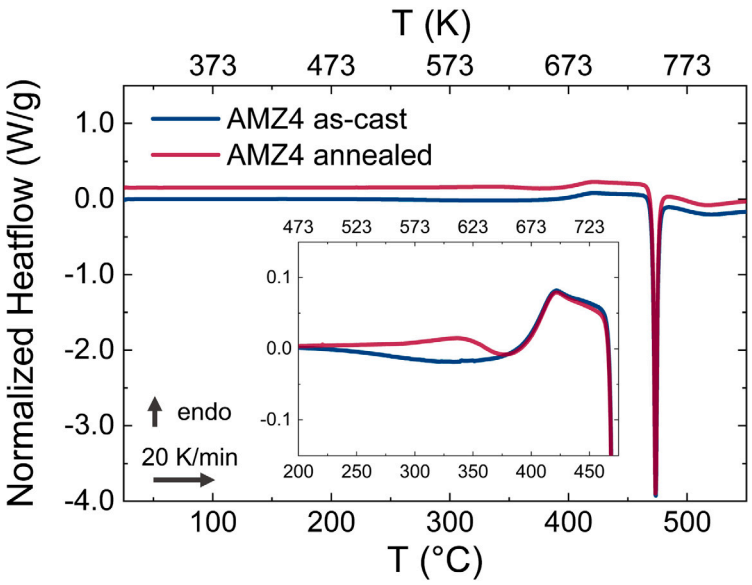

Fig. 2. Heatflow obtained by DSC of as-cast (blue) and annealed (red) AMZ4 during heating at 20 K/min, confirming the glassy state. In the main diagram, the curve for the annealed sample is shifted by +0.15 for better visibility. The glass transition temperature of as-cast AMZ4 is measured at $T_g = 401°C$, crystallization starts at $T_x^{onset} = 467°C$ and the crystallization peak temperature is obtained at $T_x = 474°C$. The sample that was annealed for 4 hours at 275°C (0.8 T_g) shows the glass transition at $T_g = 403°C$ and the onset of crystallization at $T_x^{onset} = 471°C$.

The normalized variance yields information on higher-order structural correlations, enabling the determination of MRO in amorphous materials [31].

NBDPs were recorded using a CCD camera (Gatan, US 2000) with a camera length of 1 m, employing a binning of 4 (512 × 512 pixels) and an acquisition time of 4 s. The probe current was adjusted to 15 pA. VR-FEM measurements were performed at room temperature with a total of 10 probe sizes between 0.8 nm and 5.0 nm (FWHM of Gaussian intensity beam profiles). Series of 100 NBDPs (10 × 10) were recorded in (50 × 50) nm-sized regions, which had a thickness of 0.65 t/λ (51 nm). During *in situ* heating, NBDP were obtained at elevated temperatures using a probe size of 0.91 nm in regions with a thickness of 0.7 t/λ, while all other measurement parameters remained unchanged. This was done after holding each temperature for 4.5 h, during which the ECM data was acquired at a different sample position. The high angle annular dark field signal (HAADF, Fishione Model 3000), measured simultaneously during all FEM measurements, did not show a count gradient, thereby confirming the uniform thickness of the measurement areas [37]. Normalized variances were obtained using the annular mean of variance image approach [38], and the quantitative evaluation was carried out using two different models. First, according to the Stratton–Voyles model [34], the maximum of the normalized variance of the first peak $V_{max}(R)$ (obtained from Gaussian fits) was plotted against $1/R^2$. With this, MRO parameters can be determined and different correlation lengths can be distinguished [39]. Second, the pair-persistence analysis (PPA) approach by Gibson et al. [40], valid if one MRO correlation length prevails in the amorphous structure [33,39], was employed to extract a characteristic correlation length scale Λ from the slope m and intercept c of a linear fit to the plot of Q^2/V versus Q^2 as in

$$\frac{Q^2}{V(k,Q)} = mQ^2 + c, \tag{2}$$

where Q is $0.61/R$ and $\Lambda = \frac{1}{2\pi}\sqrt{\frac{m}{c}}$.

$V(\vec{k}, R)$ is directly related to the degree of order within the examined volume, but it is also influenced by factors such as cluster size, strain within the material, the volume fraction of ordered regions, and the type of atoms involved in scattering [34,41]. Thus, interpreting $V(\vec{k}, R)$ is inherently challenging and the various factors influencing normalized variance are thoroughly discussed to account for these complexities. Moreover, as noted by Bogle et al. [41], either the peak height or the peak integral of the variance provides a semi-quantitative estimate of the MRO volume fraction.

2.4. Electron correlation microscopy, measurement parameters and data analysis

Electron correlation microscopy (ECM) measures the structural relaxation dynamics in metallic glasses by analyzing the intensity changes of the speckles in tilted dark-field (DF) TEM images over time [21,22]. The approach is based on steady-state measurement conditions [42,43], which can be confirmed by calculating two-time correlation functions (TTCF)

$$g_2(t_1, t_2) = \frac{\langle I_{t_1} I_{t_2} \rangle}{\langle I_{t_1} \rangle \langle I_{t_2} \rangle}, \tag{3}$$

where I are the pixel intensities at times t_1 and t_2 and $\langle ... \rangle$ denotes the average over all pixels in the respective DF image [22,44]. The evaluation of ECM dynamics includes the calculation of an auto-correlation function

$$g_2(t) = \frac{\langle I(t')I(t'+t) \rangle}{\langle I(t') \rangle^2}, \tag{4}$$

where pixel-wise intensities I at time t' are correlated with the intensities at a later time $I(t'+t)$, which can vary depending on the underlying dynamics [42,45]. This curve $g_2(t)$ can be calculated for every pixel in the DF images, giving a map of structural dynamics, or it can be averaged over the size of the image. Thus, $g_2(t)$ describes how long a specific atomic structure in the material, corresponding to the speckles in the DF images, exists before it changes [22]. To extract quantitative dynamics parameters, namely the structural decay time τ and stretching exponent β, the auto-correlation function is described by a Kohlrausch–Williams–Watts (KWW) function $g_2(t) = 1 + A \cdot exp\left[-2\left(\frac{t}{\tau}\right)^{\beta}\right]$, as often done for metallic glasses [13,21,46,47], and with A being an instrument-dependent scaling parameter.

The DF images recorded here were generated by tilting the incident beam and choosing the first diffraction ring to form the image with a 10 μm objective aperture. Time series of DF images 1k ×

1k were recorded on a complementary metal–oxide–semiconductor (CMOS) camera (Ceta, 4k × 4k) using a binning of 4 at a magnification of 340k for all measurements. At room temperature, the measurement protocol described previously [22] was followed, where a time interval of 5 s was chosen between two recorded DF micrographs. This included an exposure time of 4 s and a pause of 1 s between exposures, allowing for active drift correction (beam shift) by an Protochips AXON™ system. This drift correction procedure ensures that the sample remains consistently positioned throughout the measurement process. In total, 5000 frames (25 000 s) were recorded with a dose rate of $1.5 \cdot 10^5$ $e^-/(nm^2\ s)$. During *in situ* heating, the protocol was adapted to an exposure time of 1 s followed by a 1 s pause to exclude drift effects in single frames. To compensate for signal loss due to shorter dwell time, the dose rate was increased to $4.4 \cdot 10^5$ $e^-/(nm^2\ s)$. At this point, it is worth noting that the electron beam significantly influences the dynamics observed during ECM, enabling measurements at low temperatures (e.g. room temperature) compared to the glass transition temperature of the investigated BMG. However, the dynamics obtained through ECM is comparable to those of the XPCS measurements when extrapolated to longer measurement times and a zero electron dose rate, effectively negating the influence of the electron beam [22]. Hence, results from room temperature measurements cannot be easily compared to results from *in situ* experiments due to their difference in the dose rate used. Each *in situ* ECM measurement was conducted on a fresh sample region that had not been previously exposed to the electron beam. Measurements were taken after a waiting period of 2000 s to allow the system to equilibrate and for drift to stabilize. For practical reasons, the ECM heating experiments were performed over several days. Between measurement sessions, the sample was cooled to room temperature at a rate of −50 K/min to lock in the current configurational state. This cooling process was performed twice in total — once after heating to 100°C and again after heating to 200°C. For a detailed description of the *in situ* heating measurement protocol, see Fig. A.9 in the Appendix. All measurement positions had a thickness of about $0.7 - 0.9\ t/\lambda$, where thickness effects on ECM parameters τ and β are negligible [21]. The evaluation of all recorded time series included post-measurement drift correction, calculation of TTCFs and autocorrelation functions g_2, logarithmic resampling of g_2 in time, and fitting KWW to autocorrelation curves to extract the dynamics parameters τ and β. These steps are described in detail in [22], which also demonstrates that drift exceeding 5 nm, i.e. speckle movements in the DF image series, results in measurable changes in the observed dynamics, characterized by shorter decay times and evident in the TTCF maps.

3. Results

3.1. Local structure

At room temperature, VR-FEM measurements were performed on both the as-cast and annealed samples using similar experimental parameters. The DSC curves of these two sample states are given in Fig. 2, revealing different enthalpic states as changes in the glass transition signal during subsequent heating measurements. Normalized variance profiles are the result of statistical analyses of the recorded NBDPs, which are presented in Fig. 3(a) for the as-cast sample and Fig. 3(b) for the annealed sample. Both samples exhibit two peaks across all probe sizes. The initial peak, occurring at approximately $k_{max} = 4.27\ nm^{-1}$ (dotted line), corresponds to the first maximum of the normalized variance V_{max}. For probe sizes larger than 4 nm, a splitting of the first peak in the normalized variance becomes apparent in both sample states, which is not resolved in the Gaussian fits to the first maximum of normalized variance. In the as-cast state, two distinct peaks appear to develop at approximately $4.176\ nm^{-1}$ and $4.347\ nm^{-1}$, while in the annealed sample, the splitting occurs at $4.108\ nm^{-1}$ and $4.278\ nm^{-1}$. The second maximum of normalized variance, referred to as $V_{max,2}$, is observed around $k_{max,2} = 7.24\ nm^{-1}$. The heights of the respective peaks, V_{max} and $V_{max,2}$, vary with probe size, with the highest normalized variances obtained at the first peak for probe sizes of about (1.3–1.5) nm in both samples. The peak height ratio $V_{max,2}/V_{max}$, which provides information on the anisotropy or strain of amorphous materials [41,48], remains consistent across both sample states (see Fig. A.10 in the Appendix). It fluctuates around 0.40 ± 0.04, with particularly similar values for probe sizes greater than 4 nm, where peak splitting in normalized variance profiles was previously indicated.

Focusing on the evolution of the first maximum V_{max}, determined by Gaussian fits, with varying probe size R, we present the Stratton–Voyles plot shown in Fig. 3(c). For both sample states, namely, as-cast (blue, filled symbols) and annealed AMZ4 (red, hollow symbols) - this graph reveals an increase in normalized variance V as the probe size R decreases (or equivalently, as $1/R^2$ increases), peaking at approximately (1.3 ± 0.2) nm. This peak position corresponds to the dominant MRO correlation length. For even smaller probe sizes, the normalized variance subsequently decreases for both sample states. In general, the normalized variance for the annealed sample appears to be slightly higher than that of the cast sample, with an average difference of approximately 4%.

The results of the PPA are plotted in Fig. 3(d). Here, only data points larger than the maximum of the Stratton–Voyles graph are considered. The data of both samples were fitted with a linear function. For the as-cast state, a slope of $m = 5.64$ and an intercept of $c = 0.074$ were determined, resulting in a correlation length scale of $\Lambda_{as-cast} = (1.39 \pm 0.05)$ nm. The correlation length is very similar to that obtained by the Stratton–Voyles approach (1.3 ± 0.2) nm. For the annealed sample state, a correlation length scale of $\Lambda_{annealed} = (1.35 \pm 0.12)$ nm results from the slope $m = 5.45$ and intercept $c = 0.076$ of the linear fit. Here, $\Lambda_{annealed}$ is also comparable to the results obtained from the Stratton–Voyles analysis.

During *in situ* heating experiments, NBDPs were acquired at both room temperature and the corresponding elevated temperatures. This was done on a second as-cast sample suitable for heating with a probe size of $R = 0.91$ nm. After each measurement temperature was reached, it was held for 4.5 h. Experiments with other probe sizes or VR-FEM measurements were not obtained at elevated temperatures due to significant drift effects, which hindered additional measurements. The normalized variance profiles obtained from the statistical analysis of 100 NBDPs recorded at each of the six measurement temperatures between room temperature and 275°C are shown in Fig. 4(a). For all temperatures, these curves show two peaks V_{max} and $V_{max,2}$, as already obtained during room temperature measurements (see Fig. 3). At the maximum temperature of 275°C, a shoulder is observed in the normalized variance at approximately $5.3\ nm^{-1}$. Moreover, the second peak, $V_{max,2}$, appears broader than at lower temperatures, suggesting a potential splitting of the normalized variance peak into two distinct features. Gaussian fits to the first peak of normalized variance at each temperature are used to compare the obtained V_{max} during *in situ* heating. For all temperatures, these values are lower than those measured with the VR-FEM measurements at room temperature. In particular, the normalized variance measured here on the thick sample position of an as-cast state before heating is below 0.13 (Fig. 4(b)), while the value of the as-cast sample measured during VR-FEM was 0.16 (cf. Fig. 3(c)). This deviation of 23% can be attributed to the thicker sample position used for FEM measurements at higher temperatures. Nevertheless, all measurements during heating were performed on similarly thick positions and are therefore comparable with each other. Fig. 4(b) shows the evolution of the maximum normalized variance of the first peak with increasing temperature. An increase of the normalized variance from room temperature (25°C) to 150°C can be observed, with a relative change of the maximum normalized variance of 10%. At higher temperatures from 150°C up to 275°C, the maximum of the first peak of the normalized variance does not change significantly.

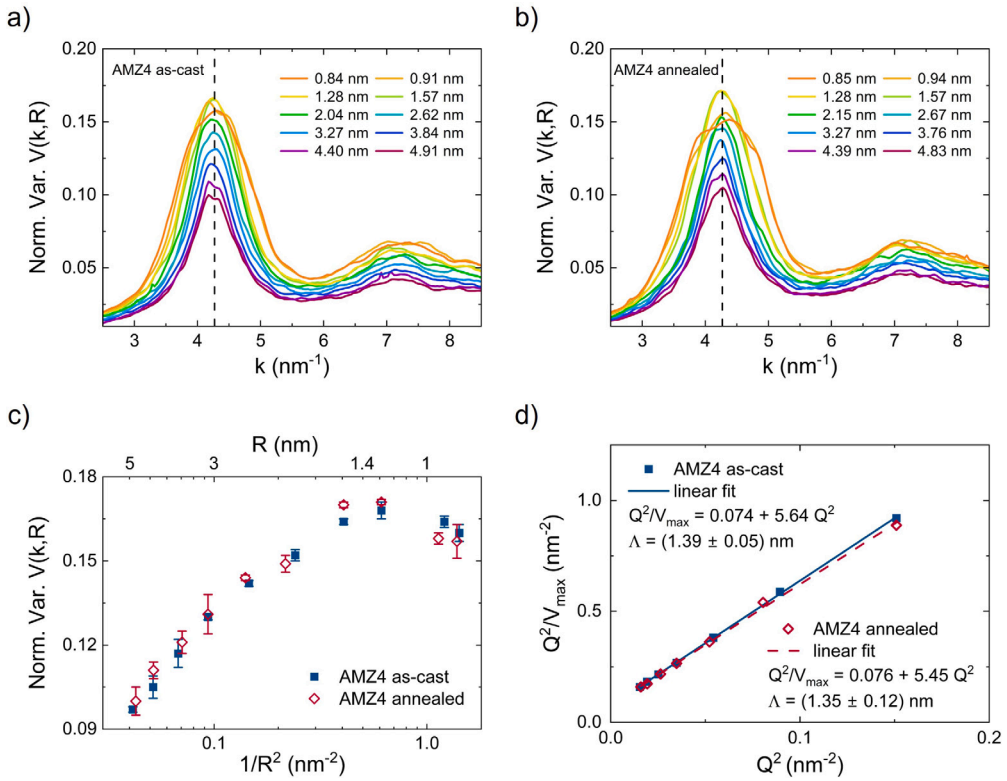

Fig. 3. Statistical analyses of NBDPs acquired at room temperature on 0.65 t/λ (51 nm) thick sample positions yielded normalized variance profiles for as-cast AMZ4 (a) and for an annealed sample state (b). The various probe sizes R used for VR-FEM measurements are given in the insets and the dotted lines indicate the position of the first maximum of the normalized variance at k_{max} = 4.27 nm^{-1}. An evaluation of the normalized variances using the Stratton–Voyles approach [34] is shown in (c). The maximum normalized variances obtained from the above profiles are plotted against the probe size for as-cast AMZ4 (blue, filled symbols) and the annealed sample state (red, hollow symbols). Error bars display the uncertainties from Gaussian fits to the peaks. The estimation of the correlation length Λ using the pair-persistence analysis according to Gibson et al. [40] is shown in (d) for the as-cast (blue, filled symbols) and the annealed sample state (red, hollow symbols).

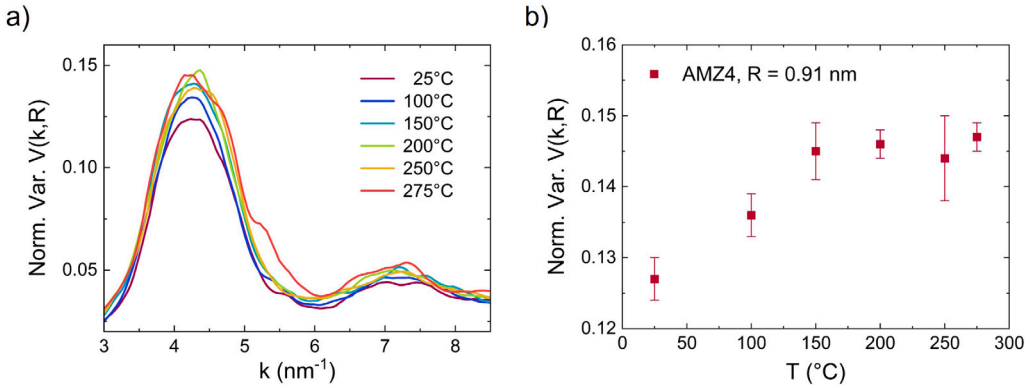

Fig. 4. Results from *in situ* heating FEM analyses on AMZ4 on 0.7 t/λ thick regions. (a) Normalized variance profiles of AMZ4 acquired with a probe size of 0.91 nm at six different temperatures. (b) Maximum normalized variances obtained from Gaussian fits to the peaks of the profiles on the left at around 4.29 nm^{-1}. Error bars are uncertainties from Gaussian fits.

3.2. Local dynamics measured at ambient temperature

ECM measurements conducted on as-cast and annealed AMZ4 glass specimens at room temperature reveal stable dynamics that are not corrupted by drift (cf. [22]), as evidenced by the stable width of the diagonal in the two-time correlation functions (TTCFs) presented in Fig. A.11 in the Appendix. These dynamics are quantitatively assessed through Kohlrausch–Williams–Watts (KWW) fits applied to the auto-correlation functions. In total, five measurement durations were selected for a series of dark field (DF) images, with the maximum duration extending to 25 000 s, which corresponds to 5000 frames of DF images each exposed for 5 s.

The structural dynamics parameters, specifically the relaxation time τ and the stretching exponent β, derived from the KWW fits are summarized in Fig. 5(a) for the as-cast state and Fig. 5(b) for the annealed state. The values of τ (represented by blue squares) for the five respective measurement durations are comparable for both samples and exhibit an increase with longer measurement durations in both states. This behavior aligns with an asymptotic function, and extrapolation to infinitely long measurement durations yields $\tau_{asym,as-cast}$ = (892 ± 12) s and $\tau_{asym,annealed}$ = (905 ± 13) s for the as-cast and annealed states,

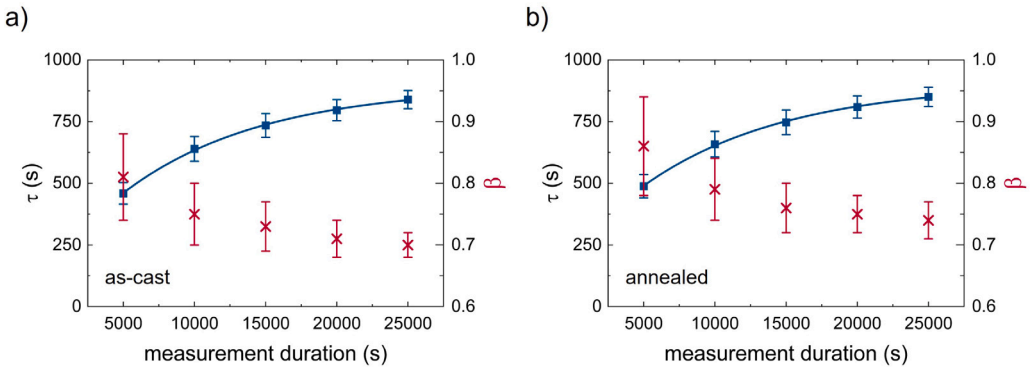

Fig. 5. Structural relaxation time τ (blue squares) and stretching exponent β (red crosses) evaluated for different measurement durations on the data acquired at room temperature on as-cast AMZ4 (a) and on a sample that was annealed as bulk material at 275°C for 4 h before the ECM measurement (b). Asymptotic extrapolation yields a structural decay time of $\tau_{asym,as-cast} = (892 \pm 12)$ s for the as-cast state and $\tau_{asym,annealed} = (905 \pm 13)$ s for the annealed sample state.

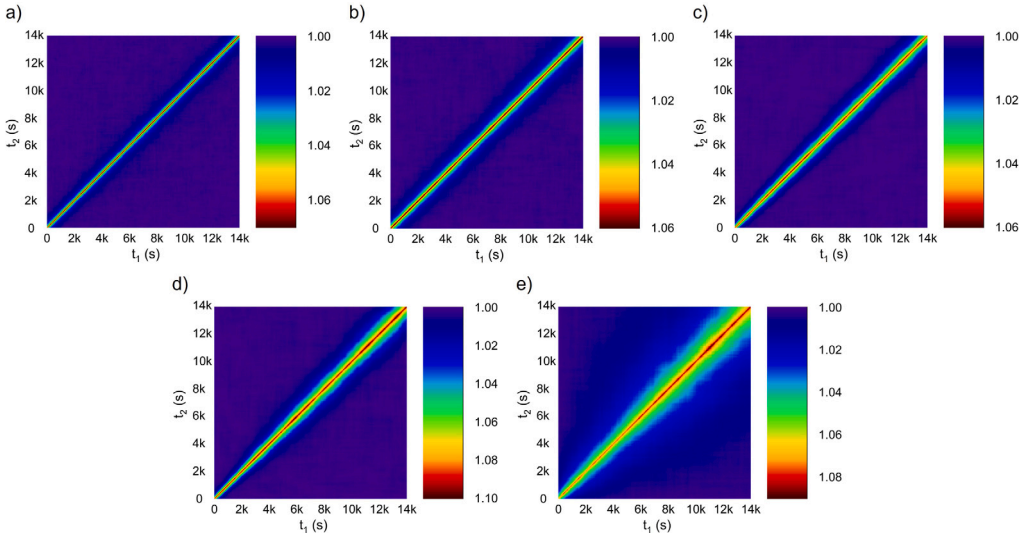

Fig. 6. Two-time correlation functions (TTCFs) obtained from *in situ* heating ECM measurements on as-cast AMZ4 at 100°C (a), 150°C (b), 200°C (c), 250°C (d), and 275°C (e).

respectively. The uncertainties indicated are fitting uncertainties. The stretching exponent β (illustrated by red crosses) shows a decrease with longer durations, ultimately stabilizing around 0.70 for the as-cast state and around 0.74 for the annealed state. Thus, both sample states demonstrate remarkably similar dynamics at room temperature with respect to the time scales of structural dynamics (τ), local dynamic mechanisms (β), and the evaluation of these parameters as the duration of measurement increases (τ_{asym}).

3.3. Local dynamics measured in-situ at elevated temperatures

In addition to the ECM measurements at room temperature, the local dynamics of an as-cast AMZ4 specimen was investigated *in situ* at elevated temperatures. Data were collected over a duration of 14000 s, beginning 2000 s after each target measurement temperature was reached and once the thermal drift had stabilized. Fig. 6 displays the TTCFs recorded during *in situ* heating experiments. The consistent width of the TTCF diagonal for measurements conducted at 100°C (a) and 150°C (b) indicates stable dynamics for the entire measurement period. As the measurement temperature rises, the width of the diagonals expands, suggesting a slowdown in dynamics. Furthermore, for the measurements conducted at 200°C (c), 250°C (d), and 275°C (e), the width of the TTCF diagonals begins to continuously broaden throughout the measurement duration, with the most pronounced effect observed at the highest temperature.

Table 1
Structural decay times τ and stretching exponents β obtained from 14 000 s long ECM measurements during *in situ* heating experiments. The room temperature (25°C) results stem from an extract of the as-cast measurement presented above.

Temperature T (°C)	Structural decay time τ (s)	Stretching exponent β
25	734	0.73
100	485	0.68
150	743	0.70
200	886	0.83
250	1023	0.84
275	1585	0.74

The widening of the TTCF diagonal is indicative of an increase in the structural decay time τ as temperature rises, even for the same measurement durations. The actual dynamics parameters are derived from KWW fits applied to the auto-correlation functions and are compiled for each image series in Table 1. These parameters are further illustrated in Fig. 7(a).

This Fig. 7(a) illustrates a modest decrease in the relaxation time at the beginning of the measurement series, where τ (represented by blue squares) decreases from 734 s at room temperature to 485 s at 100°C. Both values stem from measurement series evaluated after a duration of 14000 s; however, the room temperature measurement

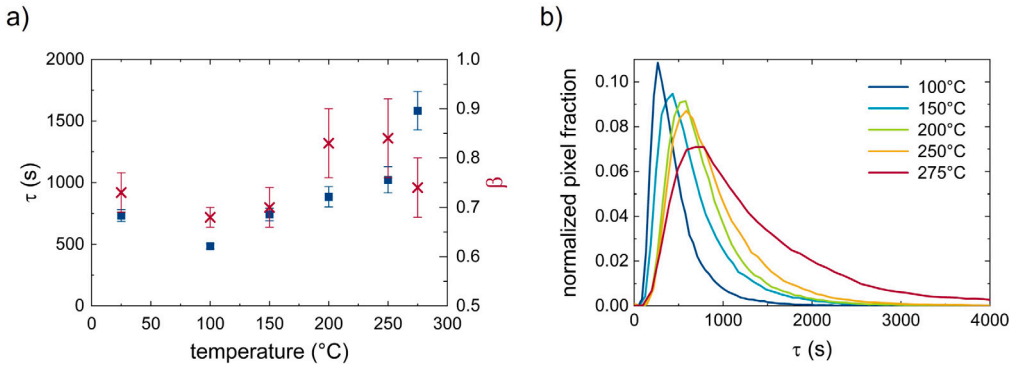

Fig. 7. (a) Structural relaxation times τ (blue squares) and stretching exponents β (red crosses), as obtained from KWW fits to ECM data recorded on as-cast AMZ4. Uncertainties are KWW fitting uncertainties. All values above room temperature (25°C) are obtained after 14000 s measurement duration. (b) Normalized pixel fractions as extracted from spatially resolved τ-maps of *in situ* ECM measurements showing increasing decay times with increasing temperature.

(presented above) was conducted on the as-cast sample for ambient temperature investigations utilizing a threefold higher electron dose rate. In contrast, for measurements conducted at temperatures above 100°C, the structural relaxation time τ exhibits an increase with increasing temperature. This trend is particularly notable at the highest temperatures, where τ increases from 1023 s at 250°C to 1585 s at 275°C. The stretching exponents β (represented by red crosses) remain consistently around 0.74 within the uncertainty of the KWW fitting for most measurements. The exception is the measurement at 100°C, where β decreases to approximately 0.68. Importantly, variations in β values during the KWW fitting process did not affect the obtained structural relaxation times τ.

To improve the assessment of the dynamics, we conducted a pixel-wise analysis within the designated measurement regions. This involves calculating the pixel-wise g_2 values and fitting the data to the KWW model [42]. This approach yields maps depicting spatially resolved dynamic parameters as shown in Fig. 8. These τ-maps highlight regions with consistent dynamics and demonstrate a uniform increase in decay time as temperature rises, rather than exhibiting localized changes, although at the highest temperature certain pixels in the map still display comparably long relaxation times (dark areas). Additionally, we can assess the pixel fraction of individual decay times τ for each temperature from these maps, as shown in Fig. 7(b). This graph provides evidence of a temperature-induced increase in decay time and indicates that a larger number of pixels exhibit slower dynamics at elevated temperatures. Furthermore, the pixel fractions demonstrate single log-normal distributions across all temperature levels.

4. Discussion

4.1. Local structure of pre-set sample states

The room temperature local structure analysis in the Zr-based BMG AMZ4 was performed on an as-cast and an annealed sample. The investigation revealed similar trends in the normalized variance, characterized by peaks at V_{max} and $V_{max,2}$, without any observable shift in k space for either sample state. When comparing the peak heights V_{max} from VR-FEM measurements, the Stratton–Voyles analysis demonstrates that both sample states exhibit an MRO correlation length of (1.3 ± 0.2) nm. An alternative analysis approach known as PPA corroborated that the characteristic correlation lengths are similar for the two glass states. Specifically, the correlation length was measured to be $\Lambda_{as-cast}$ = (1.39 ± 0.05) nm for the as-cast state and $\Lambda_{annealed}$ = (1.35 ± 0.12) nm for the structurally relaxed state. These results are consistent with those reported by Hilke et al. who observed a comparable correlation length in an as-cast Zr-based BMG with a slightly different composition ($Zr_{52.5}Cu_{17.9}Ni_{14.6}Al_{10}Ti_5$ (at.-%) - Vitreloy 105) [17]. In a study by Best et al. a Zr-based BMG with the identical composition, fabricated via additive manufacturing, was investigated [18]. However, the PPA approach revealed longer correlation lengths in the range of (1.6–1.8) nm. We attribute this discrepancy to the additive manufacturing process employed by Best et al. [18], which is known to introduce variations in density and distinct relaxation states within the sample. These differences arise from the inherent nature of manufacturing and may also lead to partial crystallization, thereby influencing the material's structure [49]. Furthermore, it is important to note that the thermal treatment applied to the annealed sample in our study cannot be directly equated with the various enthalpic states that develop during the additive manufacturing process used by Best et al. [18].

In addition to the MRO size derived from model analyses, a more detailed evaluation of the normalized variance curves is possible. The first maximum of normalized variance, denoted as V_{max}, was observed at a position of 4.27 nm^{-1} for probe sizes below 4 nm. For larger probe sizes, indications of peak splitting appear in both the as-cast and annealed state. This splitting of the first peak of normalized variance may suggest a structural change within the material. Similar phenomena have been reported in Vitreloy 105 [17] and in ZrCuAl BMG [50,51], where the first peak splits into two features at approximately 4.5 nm^{-1} and 3.7 nm^{-1} after deformation. These features have been attributed to icosahedral-like and crystal-like atomic clusters, respectively. In the present study, however, the observed splitting is less pronounced and appears to be only a tentative indication, as it is minor relative to the effects reported in the literature. Hence, the variation of the normalized variance with probe size and sample state may indicate a change in the nature of the MRO, even though the MRO sizes identified by the Stratton–Voyles and PPA analyses remain similar in both states.

The Stratton–Voyles analysis further indicates an increase in the variance signal for the annealed sample relative to the as-cast material. To gain deeper insights into the microstructural state of the amorphous samples, the peak height ratio of the second to the first peak, $V_{max,2}/V_{max}$, was examined and compared with that of the as-cast counterparts with similar composition [41] (see Fig. A.10 in the Appendix). This approach suggests that strain enhances damping at higher k values. The observed peak height ratios are comparable between the two samples across the investigated probe sizes, particularly for the probe sizes above 4 nm, where indications of peak splitting in the normalized variance profiles may occur. This implies that the annealing procedure does not significantly induce or relieve strain nor alter the MRO size, a conclusion consistent across both sample states. However, using the peak height of the variance as a semi-quantitative measure of the MRO volume fraction, the slight increase in V_{max} observed in the annealed sample can be attributed to an actual increase in the MRO volume fraction. This enhancement in the MRO volume fraction with annealing agrees well with findings from other studies on different BMG systems [52,53], supporting the notion that the material undergoes structural relaxation involving measurable structural

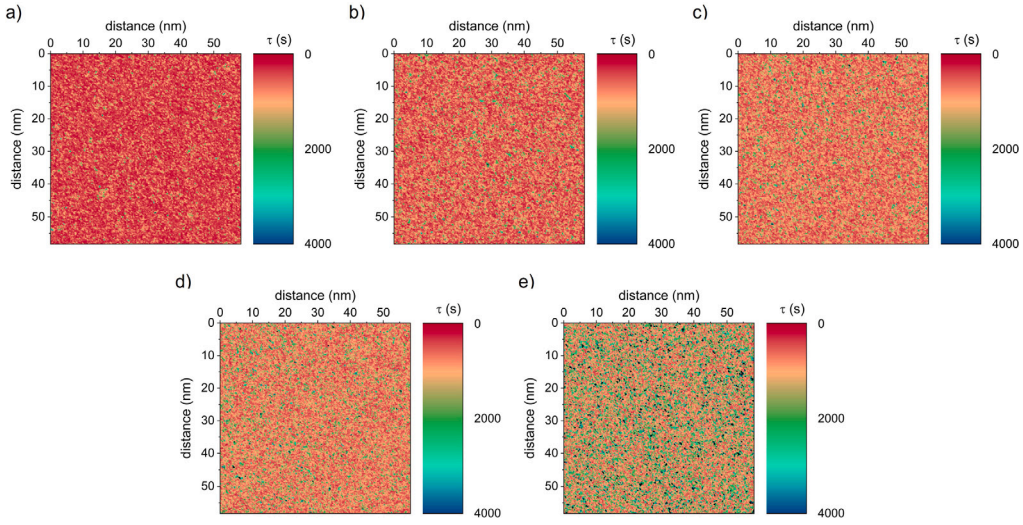

Fig. 8. Maps of spatially resolved τ values as obtained from pixel-wise calculation of auto-correlation functions g_2 and KWW fitting for the *in situ* heating ECM measurements performed at 100°C (a), 150°C (b), 200°C (c), 250°C (d), and 275°C (e). The color change in these maps shows an increase in τ with increasing temperature, i.e. a slowing down of dynamics, which is not spatially confined but uniformly distributed over the entire measurement area.

changes in the MRO volume fraction. Interestingly, the MRO correlation lengths determined for both sample states are essentially equal, indicating that the nature of MRO remains unaffected by structural relaxation. This contrasts with observations in pre-annealed Pd-based BMG (e.g. $Pd_{40}Ni_{40}P_{20}$ (at.-%)), where both the MRO correlation length and volume fraction change by pre-annealing, i.e. in structurally relaxed samples [48,52]. The differing effects of structural relaxation on the MRO may be related to the fragility of the materials. PdNiP is a more fragile glass than AMZ4, and by definition, higher fragile corresponds to more pronounced thermally induced variation in the MRO structure [54]. Consequently, it appears that the AMZ4 BMG retains its MRO characteristics during relaxation, a behavior likely linked to its lower fragility compared to PdNiP.

4.2. Structural changes during in situ heating

The *in situ* NBDPs acquired during heating of an as-cast TEM sample employed a probe size of $R = 0.91$ nm, with measurement locations selected to correspond to a sample thickness of 0.7 t/λ. Compared to measurements on as-cast and pre-annealed sample states performed at room temperature (Fig. 3), the normalized variances observed during heating were reduced (Fig. 4), primarily due to differences in sample thickness. Nevertheless, the measurement parameters remained consistent throughout the heating experiment, ensuring the comparability of the results.

During *in situ* heating, a total relative increase of 10% was observed in the normalized variance as the temperature rose. An increase in MRO suggests that the spatial arrangement of atoms or clusters becomes more correlated with rising temperatures. This is evidenced by the increase in V_{max} shown in Fig. 4(b), which reflects an expansion in the MRO volume fraction. The most significant changes occurred at lower temperatures, with notable variations as the temperature increased from room temperature up to 150°C. Beyond this point, from 150°C to 275°C, the height of the normalized variance at the first peak remained essentially unchanged, indicating no substantial structural alterations and thus may be attributed to the completion of structural transformations. The increase in MRO up to approximately 150°C can be attributed to the fact that the pristine amorphous structure is relatively less ordered in terms of MRO. The growth of MRO is a thermally activated process that approaches saturation near 150°C. This behavior appears to be linked to the onset of faster dynamics observed around 100°C, as indicated by the ECM experiments in Fig. 7(a). However, fully elucidating the relationship between structural evolution and dynamic behavior is complex; therefore, we refrain from making definitive claims about their interconnection.

It is worth noting that the shape of the normalized variance curves evolves with increasing temperature, especially at the highest temperature investigated, 275°C. At this temperature, a pronounced feature emerges at approximately 5.3 nm^{-1}, exhibiting a higher normalized variance compared to lower temperatures. This could suggest potential structural modifications, such as the formation of new phases or the splitting of an existing peak. While this may point toward the formation of crystal-like atomic clusters, a phenomenon observed in other Zr-based BMGs [17,50,51], alternative explanations—such as the onset of quasi-crystalline structures or partial crystallization—could also be possible. However, the absence of definitive crystalline signatures in the selected area diffraction mapping at elevated temperatures does not fully support the presence of crystalline phases. This limitation suggests that if structural changes are occurring, they may not involve long-range ordering typical of crystalline materials. The slight broadening observed in the second peak of the normalized variance could indicate the presence of such structural modifications, but the exact nature of these changes remains unclear without further evidence.

The absence of VR-FEM measurements precludes performing Stratton–Voyles analysis and PPA, limiting insights into the MRO correlation length during *in situ* heating. Consequently, other local structural changes at different length scales – beyond the scope of this study – may have transpired during *in situ* heating. Conducting further experiments focused on these scales could yield a more comprehensive understanding of the local structure evolution and the potential formation of quasi-crystalline phases during *in situ* heating.

Despite this, the current data enable a meaningful discussion of the observed variations in the normalized variance as a function of increasing FEM measurement temperature. This is significant because the normalized variance is related to the temperature dependence of the relative volume fraction of MRO, with a length scale determined by the probe size. If we assume that the observed trend is representative across the entire spectrum of MRO correlation lengths, then these data could potentially be used to establish correlations with macroscopically averaging quantities – such as fragility – similar to what is suggested by VR-FEM results at room temperature.

Furthermore, this overall increase in the normalized variance during *in situ* heating was already suggested by room temperature VR-FEM results obtained on both as-cast and a pre-annealed samples. However,

the relative variance increase was lower (4%) for the room temperature measurements on a sample that had undergone thermal annealing as a bulk before TEM lamellae preparation. The discrepancy may be attributed to thin foil effects [55]. Despite these differences, both measurement sets – those on pre-conditioned samples and those during heating – demonstrate a consistent trend of increasing normalized variance with ongoing structural relaxation. To our knowledge, this is the first report confirming the rise in normalized variance with annealing in a BMG sample through *in situ* electron microscopy.

4.3. Dynamics of pre-conditioned samples

At room temperature, ECM measurements reveal similar stable dynamics for both investigated glassy states of AMZ4 — whether in the as-cast or annealed condition. This consistency is observed across all five measurement durations, including the decay times τ, the extrapolated decay times τ_{asym}, and the stretching exponents β. These findings indicate that the two configurational states are indistinguishable by room temperature ECM measurements, contrasting with the results from XPCS reported by Lüttich et al. who observed an increase in τ upon pre-annealing [7]. As previously discussed [22], this discrepancy may be attributed to the significant influence of the electron beam on the material during ECM measurements, which accelerates the observed dynamics. It has been demonstrated that only by considering asymptotic measurement times and extrapolation to zero electron beam influence do ECM results align with those obtained via XPCS [22]. Interestingly, ECM measurements show equal asymptotic relaxation times for both the as-cast and pre-annealed samples, suggesting that both states are equally susceptible to the "forced" dynamics induced by the electron beam. This can be linked to local structural differences observed in the as-cast material versus the pre-annealed state — specifically, identical MRO correlation length scales and differing MRO volume fractions, as supported by FEM results at elevated temperatures. Thus, the observation of comparable electron beam-induced susceptibilities at room temperature implies that the nature of MRO – that is, its correlation length – rather than the volume fraction, predominately influences the local dynamics driven by the electron beam. Based on this, it can be further speculated that the intrinsic relaxation process, which are unaffected by external perturbations such as an electron beam at fixed temperature, are governed more by the type and MRO correlation length rather than its volume fraction.

4.4. Structural relaxation dynamics during in situ heating

In addition to conducting measurements at room temperature, we carried out *in situ* heating experiments on an as-cast sample utilizing a shorter frame acquisition time along with a higher electron dose rate to achieve an optimal signal-to-noise ratio. The modifications in measurement parameters during the transition from room temperature to *in situ* experiments at elevated temperatures account for the observed decrease in decay time τ from room temperature to 100°C, as shown in Table 1. Given that the measurement temperature is relatively low compared to the glass transition temperature, it is unlikely that a change in atomic mobility influences the results significantly. Instead, the electron dose rate, which was three times higher during the 100°C measurements than at room temperature, accelerates the dynamics more strongly, resulting in a decrease in τ at 100°C [22]. Despite the effects of the electron beam when its parameters are changed, the same electron beam parameters were used for all *in situ* ECM measurements. Thus, the influence of the electron beam can be assumed to be constant at each elevated measurement temperature and therefore changes in dynamics with increasing temperature should be intrinsic to the material and not due to the electron beam.

This consistent width of the TTCF at both 100°C and 150°C indicates that steady-state measurement conditions were successfully maintained [20,22]. Furthermore, the observed broadening of the TTCF width over longer measurement durations and with increasing temperatures – from 200°C to 250°C and 275°C – suggests a slowdown in dynamics indicative of ongoing structural relaxation or "aging" of the sample. This interpretation is supported by findings from XPCS data [20,56–58]. While these observations could also imply the onset of fluctuations leading to crystallization [59], diffraction patterns obtained after high-temperature measurements showed no evidence of crystallization, allowing us to exclude this possibility at lower temperatures. At 275°C, no changes were observed in the averaged selected area diffraction patterns; however, nanobeam diffraction pattern analysis reveals local structural modifications. Therefore, the increase in the decay time τ with rising measurement temperature primarily results from structural relaxation. However, the pronounced increase in τ at the highest temperature may also involve an additional effect, such as structural transition – potentially partial crystallization – as discussed in Section 4.2. While this effect cannot be precisely quantified, it appears to be reflected in the spatially resolved τ-maps, where pixels occur exhibiting comparatively long decay times are observed (see below).

Thus, the increasing structural decay times τ observed through *in situ* heating ECM measurements highlight the structural relaxation processes in the material during annealing and may involve effects such as structural transitions at higher temperatures. The decreasing dynamics trends with increasing temperature and time suggest ongoing structural relaxation during heating and potentially structural transitions at higher temperatures. During relaxation at elevated temperatures, local dynamics characterized by the relaxation times τ can exhibit significant, transient variations on the nanometer scale. As the relaxation speed or temperature increases, these spatial fluctuations become more pronounced, as shown in Fig. 8. However, in fully relaxed materials, such variations tend to diminish. At sufficiently high temperatures—above the glass transition and approaching the undercooled melt—these heterogeneities are expected to vanish entirely. Furthermore, the influence of drift on the results can be confidently excluded, as the data were corrected for drift both during and after acquisition. The maps do not show any indications of drift, such as abrupt changes in the width of the diagonal in the TTCF maps (Fig. 6). Had there been a drift of approximately 5 nm or more, it would have led to shorter decay times [22]. However, such a drift would not account for the observed relative increase in decay times with higher measurement temperature and longer durations. These findings are consistent with previous studies by Lüttich et al. who observed an increase in decay times for metallic glasses pre-annealed below the glass transition temperature (T_g) using XPCS [7]. Additionally, the results align with thermal and mechanical experiments that report reduced atomic mobility associated with structural relaxation [60].

Previous ECM studies predominantly focused on temperatures where the material existed in a supercooled liquid state, often utilizing short frame acquisition times of less than 1 s - times that were further reduced at higher temperatures [21,45,59,61]. In these conditions, a decrease in decay times τ with increasing temperature was consistently observed, reflecting enhanced local relaxation dynamics characteristic of supercooled liquids. In this study, we adhered to a consistent frame time of 1 s across all temperature measurements to ensure an adequate signal-to-noise ratio. Due to the onset of crystallization within the TEM sample, we were unable to acquire data in the supercooled liquid state above T_g = 401°C. As a result, the temperature and temporal ranges explored do not encompass the supercooled liquid region's intrinsic relaxation dynamics. Instead, our observations pertain to the local atomic rearrangements occurring during aging processes during *in situ* measurements.

Regarding the stretching exponents β, a consistent value of 0.74 was obtained during the *in situ* measurement at 275°C and for the pre-annealed sample state at the same temperature under ambient conditions. Other β values measured at elevated temperatures do not significantly deviate from this result. However, the β value measured at 100°C is significantly lower than 0.74. This reduction may be due to a

fraction of fast and heterogeneous relaxation at this lower temperature, which differ from those at higher *in situ* measurement temperatures. Since the measurement duration of 14000 s approaches the asymptotic regime more closely for these faster dynamics, the observed β value reflects this transient behavior. As the measurement duration increases, β tends to stabilize, aligning with the asymptotic values observed at room temperature measurements in both sample states. Furthermore, variations in β during the KWW fits did not influence the derived structural relaxation times τ, indicating that the fundamental relaxation mechanism remained unchanged during the ECM measurements. Hence, the stretching exponents serves as an effective parameter for characterizing the nature of the relaxation dynamics (e.g., stretched vs. compressed). However, due to the non-uniqueness of solutions within the fitting procedure, specific β values within the same order of magnitude should not be overinterpreted.

In contrast to XPCS measurements of the annealed sample states, the ECM results presented here not only confirm the increase in τ with rising temperature and ongoing *in situ aging* but also reveal consistent aging dynamics. This stability is evidenced by the KWW parameter β, which remained constant within the fitting uncertainty across the investigated temperatures, and by spatially resolved τ-maps showing no localized anomalies. No indications of "cluster"-like atomic movements during structural relaxation were observed; instead, regions exhibit uniform dynamics characterized by a coherent increase in τ with temperature. Furthermore, the pixel-wise evaluation of τ at each temperature reveals that the distribution of decay times follows a logarithmic normal distributions that shifts toward longer times as temperature increases. The preservation of the distribution's shape across temperatures further corroborates the stability of the underlying relaxation dynamics. At the highest temperature investigated, 275°C, the increase in τ was more pronounced than at lower temperatures. The τ-map at this temperature displayed pixels with significantly longer decay times, indicating notable changes in local dynamics. While the size of the domains exhibiting relaxation times exceeding $2\tau_{g_2}$ remained unchanged during heating, the observed local structural transition – potentially signifying the onset of crystallization – is reflected in an increased intensity of pixels associated with slow decay times. This suggests that structural relaxation persists at this elevated temperature. Additionally, the data imply that further transitions affecting local structure and dynamics may occur at 275°C, highlighting the complexity of the processes active at this temperature.

On a last note, it should be mentioned that the observed subtle changes in local structure and the pronounced alterations in dynamics both likely stem from ongoing structural relaxation within the material. However, whether these phenomena are directly linked through a specific physical mechanism remains unproven. At the highest measurement temperature of 275°C, a connection appears plausible, as the dynamics slow more markedly than at lower temperatures, accompanied by notable shifts in the normalized variance pattern. However, the observed structural decay time at this temperature may also be longer, since the material could already have reached a more stable configuration during earlier isothermal holds. This increased stability is not captured in the variance signal associated with the MRO volume fraction.

5. Conclusion

Fluctuation electron microscopy measurements conducted under ambient conditions for specific sample states demonstrate consistent medium-range order (MRO) correlation lengths in both as-cast and annealed AMZ4 bulk metallic glass (BMG), as assessed by two different models [34,40]. These glassy states show variations in the variance peak height, which indicate an increasing MRO volume fraction as structural relaxation progresses/occurs during annealing. This is the first observation of a change in the normalized variance associated with structural relaxation during *in situ* heating within an electron microscope, thereby confirming and reinforcing the findings from previous room-temperature experiments conducted on well-defined sample states.

Room temperature electron correlation microscopy (ECM) reveals similar dynamics across different configurational states of the investigated BMG, established by annealing below the glass transition temperature, largely due to the significant influence of the electron beam. However, as the temperature was increased for *in situ* measurements, the dynamics of the investigated Zr-based BMG sample exhibited noticeable changes. Within the accessible time and temperature ranges, slower dynamics associated with ongoing structural relaxation were recorded as temperatures rose, substantiating findings from X-ray photon correlation spectroscopy (XPCS) conducted on pre-annealed samples. With ECM providing enhanced spatial resolution compared to XPCS, the observed aging process was uniform, affecting the sample consistently throughout the spatial measurement area. At the highest investigated measurement temperature, a more pronounced slowdown in dynamics was observed, potentially related to changes in the normalized variance. These changes may stem from local structural modifications associated with the early stages of quasi-crystal formation.

Integrating these findings in AMZ4 indicates that the structural changes that occur during heating are inherently related to the structural relaxation process, which ultimately guides the material to a more stable state characterized by slower intrinsic dynamics and increased MRO volume fraction. Based on the present measurements—limited to a single alloy composition—it appears plausible that changes during structural relaxation are associated primarily with variations in the MRO volume fraction, rather than in its type or correlation length. If this interpretation is correct, it would suggest that the type of MRO may be largely determined by the chemical composition, and thus related to the fragility of the system, rather than being substantially altered by structural relaxation itself. However, this should be regarded as a working hypothesis pending confirmation across a broader range of compositions.

CRediT authorship contribution statement

Olivia Vaerst: Writing – original draft, Visualization, Investigation, Formal analysis, Data curation, Conceptualization. **Harald Rösner:** Writing – review & editing, Validation, Supervision, Project administration. **Martin Peterlechner:** Writing – review & editing, Supervision, Project administration, Funding acquisition. **Gerhard Wilde:** Writing – review & editing, Supervision, Resources, Project administration, Funding acquisition.

Declaration of competing interest

The authors declare that they have no known competing financial interests or personal relationships that could have appeared to influence the work reported in this paper.

Acknowledgments

Financial support by Deutsche Forschungsgemeinschaft (DFG), Germany under the research grants Wi 1899/47-1 and Pe 2290/2-2 is gratefully acknowledged. The DFG is further acknowledged for funding the TEM equipment via the Major Research Instrumentation Program under INST 211/719-1 FUGG. FIB preparation was carried out at Münster Nanofabrication Facility (MNF). AI assistance available in overleaf was used for improving readability.

Appendix. Supplementary material

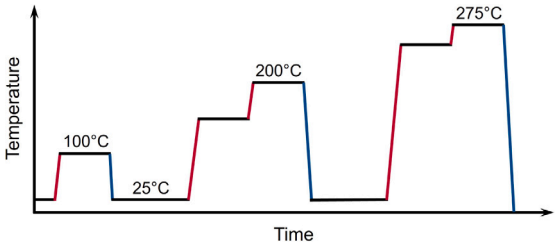

Fig. A.9. Protocol of the TEM *in situ* heating experiments performed on an as-cast AMZ4 sample showing the temperature setting over time. ECM data was acquired during isothermal holds at 100°C, 150°C, 200°C, 250°C, and 275°C. *in situ* heating NBDPs for FEM analysis were obtained during isothermal holds after ECM measurements. Heating was done at 20 K/min, cooling at 50 K/min.

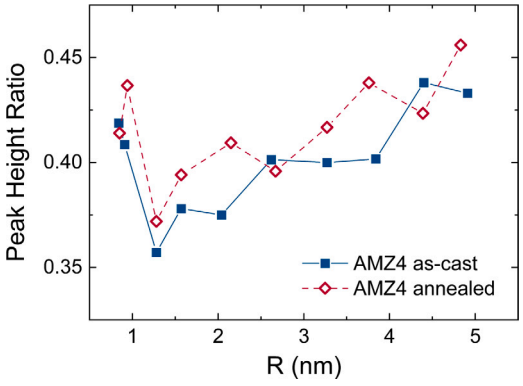

Fig. A.10. Peak height ratios of the normalized variances $V_{max,2}/V_{max}$ obtained from the normalized variance profiles shown in Fig. 3 (a, b) are plotted against the probe size R. This ratio is a measure for strain or anisotropy [48] and reveals here no significant differences between the two sample states (as cast and annealed).

References

[1] W.H. Wang, Dynamic relaxations and relaxation-property relationships in metallic glasses, Prog. Mater. Sci. 106 (2019) 100561, http://dx.doi.org/10.1016/j.pmatsci.2019.03.006.

[2] M. Goldstein, Viscous liquids and the glass transition: A potential energy barrier picture, J. Chem. Phys. 51 (1969) 3728–3739, http://dx.doi.org/10.1063/1.1672587.

[3] A. Greer, Structural relaxation and atomic transport in amorphous alloys, in: H.H. Liebermann (Ed.), Rapidly Solidified Alloys, Marcel Dekker, INC., New York, 1993.

[4] S. Scudino, M. Stoica, I. Kaban, K. Prashanth, G. Vaughan, J. Eckert, Length scale-dependent structural relaxation in $Zr_{57.5}Ti_{7.5}Nb_5Cu_{12.5}Ni_{10}Al_{17.5}$ metallic glass, J. Alloys Compd. 639 (2015) 465–469, http://dx.doi.org/10.1016/j.jallcom.2015.03.179.

[5] F.H. Stillinger, A topographic view of supercooled liquids and glass formation, Science 267 (1995) 1935–1939, URL http://www.jstor.org/stable/2886441.

[6] A. Heuer, Exploring the potential energy landscape of glass-forming systems: from inherent structures via metabasins to macroscopic transport, J. Phys.: Condens. Matter. 20 (37) (2008) 373101, http://dx.doi.org/10.1088/0953-8984/20/37/373101.

[7] M. Lüttich, V.M. Giordano, S. Le Floch, E. Pineda, F. Zontone, Y. Luo, K. Samwer, B. Ruta, Anti-aging in ultrastable metallic glasses, Phys. Rev. Lett. 120 (2018) 135504, http://dx.doi.org/10.1103/PhysRevLett.120.135504.

[8] Y. Fan, T. Iwashita, T. Egami, Energy landscape-driven non-equilibrium evolution of inherent structure in disordered material, Nat. Commun. 8 (2017) 15417, http://dx.doi.org/10.1038/ncomms15417.

[9] C.T. Moynihan, Structural relaxation and the glass transition, Rev. Miner. 32 (1995) 1–20, http://dx.doi.org/10.2138/rmg.1995.32.1.

[10] C. Mitsch, G.P. Görler, G. Wilde, R. Willnecker, Heat capacity of $Pd_{40}Ni_{40}P_{20}$ in the deeply undercooled liquid state determined by relaxation experiments in the glass transition region, J. Non-Cryst. Solids 270 (1) (2000) 172–180, http://dx.doi.org/10.1016/S0022-3093(00)00073-9.

[11] G. Wilde, G.P. Görler, R. Willnecker, H.J. Fecht, Calorimetric, thermomechanical, and rheological characterizations of bulk glass-forming $Pd_{40}Ni_{40}P_{20}$, J. Appl. Phys. 87 (3) (2000) 1141–1152, http://dx.doi.org/10.1063/1.371991.

[12] T. Egami, Structural relaxation in amorphous $Fe_{40}Ni_{40}P_{14}B_6$ studied by energy dispersive X-ray diffraction, J. Mater. Sci. 13 (1978) 2587–2599, http://dx.doi.org/10.1007/BF02402745.

[13] C. Nagel, K. Rätzke, E. Schmidtke, F. Faupel, W. Ulfert, Positron-annihilation studies of free-volume changes in the bulk metallic glass $Zr_{65}Al_{7.5}Ni_{10}Cu_{17.5}$ during structural relaxation and at the glass transition, Phys. Rev. B 60 (1999) 9212–9215, http://dx.doi.org/10.1103/PhysRevB.60.9212.

[14] H. Zhou, S. Hilke, E. Pineda, M. Peterlechner, Y. Chushkin, S. Shanmugam, G. Wilde, X-ray photon correlation spectroscopy revealing the change of relaxation dynamics of a severely deformed Pd-based bulk metallic glass, Acta Mater. 195 (2020) 446–453, http://dx.doi.org/10.1016/j.actamat.2020.05.064.

[15] B. Li, S. Xie, J.J. Kruzic, Toughness enhancement and heterogeneous softening of a cryogenically cycled Zr–Cu–Ni–Al–Nb bulk metallic glass, Acta Mater. 176 (2019) 278–288, http://dx.doi.org/10.1016/j.actamat.2019.07.012.

[16] D. Grell, F. Dabrock, E. Kerscher, Cyclic cryogenic pretreatments influencing the mechanical properties of a bulk glassy Zr-based alloy, Fatigue Fract. Eng. Mater. Struct. 41 (2018) 1330–1343, http://dx.doi.org/10.1111/ffe.12777.

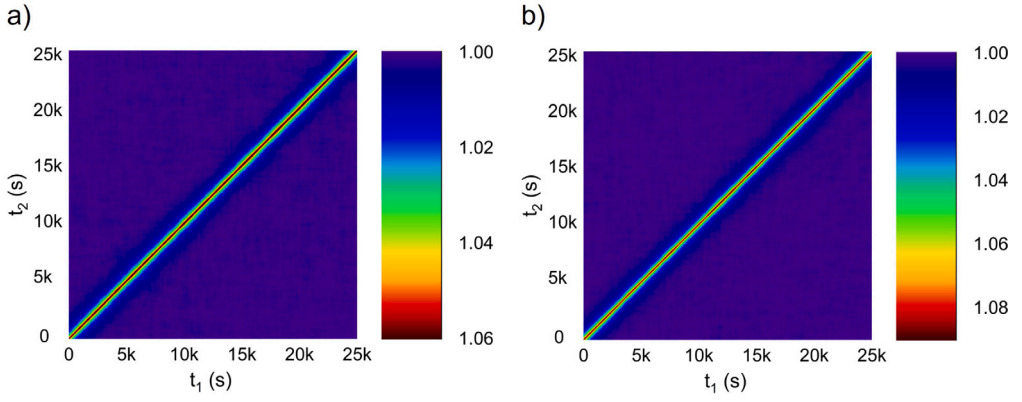

Fig. A.11. Two-time correlation functions (TTCFs) for the as-cast (a) and annealed sample (b) of AMZ4, derived from 25 000 s room temperature ECM measurements, indicate stable dynamics throughout the measurement period, as evidenced by the consistent width of the TTCF diagonals.

[17] S. Hilke, H. Rösner, D. Geissler, A. Gebert, M. Peterlechner, G. Wilde, The influence of deformation on the medium-range order of a Zr-based bulk metallic glass characterized by variable resolution fluctuation electron microscopy, Acta Mater. 171 (2019) 275–281, http://dx.doi.org/10.1016/j.actamat.2019.04.023.

[18] J.P. Best, K. Nomoto, F. Yang, B. Li, M. Stolpe, L. Zeng, Z. Evenson, C. Hugenschmidt, X. Li, S.P. Ringer, J.J. Kruzic, Advanced structural analysis of a laser additive manufactured Zr-based bulk metallic glass along the build height, J. Mater. Sci. 57 (2022) 9678–9692, http://dx.doi.org/10.1007/s10853-022-06991-6.

[19] M. Sutton, S.G.J. Mochrie, T. Greytak, S.E. Nagler, L.E. Berman, G.A. Held, G.B. Stephenson, Observation of speckle by diffraction with coherent X-rays, Nature 352 (1991) 608–610, http://dx.doi.org/10.1038/352608a0.

[20] B. Ruta, Y. Chushkin, G. Monaco, L. Cipelletti, E. Pineda, P. Bruna, V.M. Giordano, M. Gonzalez-Silveira, Atomic-scale relaxation dynamics and aging in a metallic glass probed by X-ray photon correlation spectroscopy, Phys. Rev. Lett. 109 (16) (2012) 1–5, http://dx.doi.org/10.1103/PhysRevLett.109.165701.

[21] P. Zhang, J.J. Maldonis, Z. Liu, J. Schroers, P.M. Voyles, Spatially heterogeneous dynamics in a metallic glass forming liquid imaged by electron correlation microscopy, Nat. Commun. 9 (1129) (2018) http://dx.doi.org/10.1038/s41467-018-03604-2.

[22] O. Vaerst, G. Wilde, M. Peterlechner, Beam effects on atomic dynamics in metallic glasses studied with electron correlation microscopy, Microsc. Microanal. 29 (2023) 1870–1878, http://dx.doi.org/10.1093/micmic/ozad110.

[23] L. Zrodowski, R. Wróblewski, T. Choma, T. Rygier, M. Rosiński, B. Morończyk, M. Kasonde, M. Leonowicz, J. Jaroszewicz, M. Ostrysz, W. Lacisz, P. Blyskun, K. Pomian, Ultrashort sintering and near net shaping of Zr-based AMZ4 bulk metallic glass, Mater. (Basel) 14 (19) (2021) 5862, http://dx.doi.org/10.3390/ma14195862.

[24] D. Radić, M. Peterlechner, H. Bracht, Focused ion beam sample preparation for in situ thermal and electrical transmission electron microscopy, Microsc. Microanal. 27 (4) (2021) 828–834, http://dx.doi.org/10.1017/S1431927621012022.

[25] T. Malis, S.C. Cheng, R.F. Egerton, EELS log-ratio technique for specimen-thickness measurement in the TEM, J. Electron Microsc. Tech. 8 (1988) 193–200, http://dx.doi.org/10.1002/jemt.1060080206.

[26] D.R.G. Mitchell, B. Schaffer, Scripting-customised microscopy tools for Digital Micrograph™, Ultramicroscopy 103 (2005) 319–332, http://dx.doi.org/10.1016/j.ultramic.2005.02.003.

[27] D.R.G. Mitchell, Determination of mean free path for energy loss and surface oxide film thickness using convergent beam electron diffraction and thickness mapping: A case study using Si and P91 steel, J. Microsc. 224 (2) (2006) 187–196, http://dx.doi.org/10.1111/j.1365-2818.2006.01690.x.

[28] M.M.J. Treacy, J.M. Gibson, Variable coherence microscopy: A rich source of structural information from disordered materials, Acta Crystallogr. A 52 (1996) 212–220, http://dx.doi.org/10.1107/S0108767395012876.

[29] M. Treacy, J. Gibson, L. Fan, D. Paterson, I. McNulty, Fluctuation microscopy: A probe of medium range order, Rep. Progr. Phys. 68 (12) (2005) 2899.

[30] J. Hwang, P. Voyles, Variable resolution fluctuation electron microscopy on Cu-Zr metallic glass using a wide range of coherent stem probe size, Microsc. Microanal. 17 (1) (2011) 67–74.

[31] T. Iwai, P. Voyles, J.M. Gibson, Y. Oono, Method for detecting subtle spatial structures by fluctuation microscopy, Phys. Rev. B 60 (1) (1999) 191.

[32] M. Treacy, When structural noise is the signal: Speckle statistics in fluctuation electron microscopy, Ultramicroscopy 107 (2–3) (2007) 166–171.

[33] P.M. Voyles, D.A. Muller, Fluctuation microscopy in the STEM, Ultramicroscopy 93 (2002) 147–159, http://dx.doi.org/10.1016/S0304-3991(02)00155-9.

[34] W.G. Stratton, P.M. Voyles, A phenomenological model of fluctuation electron microscopy for a nanocrystal/amorphous composite, Ultramicroscopy 108 (8) (2008) 727–736, http://dx.doi.org/10.1016/J.ULTRAMIC.2007.11.004.

[35] S.N. Bogle, L.N. Nittala, R.D. Twesten, P.M. Voyles, J.R. Abelson, Size analysis of nanoscale order in amorphous materials by variable-resolution fluctuation electron microscopy, Ultramicroscopy 110 (10) (2010) 1273–1278, http://dx.doi.org/10.1016/j.ultramic.2010.05.001.

[36] F. Yi, P. Tiemeijer, P.M. Voyles, Flexible formation of coherent probes on an aberration-corrected STEM with three condensers, J. Electron Microsc. 59 (2010) 15–21, http://dx.doi.org/10.1093/jmicro/dfq052.

[37] F. Yi, P.M. Voyles, Effect of sample thickness, energy filtering, and probe coherence on fluctuation electron microscopy experiments, Ultramicroscopy 111 (2011) 1375–1380, http://dx.doi.org/10.1016/j.ultramic.2011.05.004.

[38] T.L. Daulton, K.S. Bondi, K.F. Kelton, Nanobeam diffraction fluctuation electron microscopy technique for structural characterization of disordered materials-Application to $Al_{88-x}Y_7Fe_5Ti_x$ metallic glasses, Ultramicroscopy 110 (10) (2010) 1279–1289, http://dx.doi.org/10.1016/j.ultramic.2010.05.010.

[39] F.A. Davani, S. Hilke, H. Rösner, D. Geissler, A. Gebert, G. Wilde, Correlations between the ductility and medium-range order of bulk metallic glasses, J. Appl. Phys. 128 (2020) 015103, http://dx.doi.org/10.1063/5.0007564.

[40] J.M. Gibson, M.M. Treacy, P.M. Voyles, Atom pair persistence in disordered materials from fluctuation microscopy, Ultramicroscopy 83 (3–4) (2000) 169–178, http://dx.doi.org/10.1016/S0304-3991(00)00013-9.

[41] S.N. Bogle, P.M. Voyles, S.V. Khare, J.R. Abelson, Quantifying nanoscale order in amorphous materials: simulating fluctuation electron microscopy of amorphous silicon, J. Phys.: Condens. Matter. 19 (45) (2007) 455204, http://dx.doi.org/10.1088/0953-8984/19/45/455204.

[42] L. He, P. Zhang, M.F. Besser, M.J. Kramer, P.M. Voyles, Electron correlation microscopy: A new technique for studying local atom dynamics applied to a supercooled liquid, Microsc. Microanal. 21 (4) (2015) 1026–1033, http://dx.doi.org/10.1017/S1431927615000641.

[43] K. Spangenberg, S. Hilke, G. Wilde, M. Peterlechner, Direct view on non-equilibrium heterogeneous dynamics in glassy nanorods, Adv. Funct. Mater. 31 (38) (2021) 2103742, http://dx.doi.org/10.1002/adfm.202103742.

[44] M. Sutton, K. Laaziri, F. Livet, F. Bley, Using coherence to measure two-time correlation functions, Opt. Express 11 (2003) 2268–2277, http://dx.doi.org/10.1364/OE.11.002268.

[45] P. Zhang, L. He, M.F. Besser, Z. Liu, J. Schroers, M.J. Kramer, P.M. Voyles, Applications and limitations of electron correlation microscopy to study relaxation dynamics in supercooled liquids, Ultramicroscopy 178 (2017) 125–130, http://dx.doi.org/10.1016/j.ultramic.2016.09.001.

[46] S.H. Chung, J.R. Stevens, Time-dependent correlation and the evaluation of the stretched exponential or Kohlrausch–Williams–Watts function, Am. J. Phys. 59 (1991) 1024–1230, http://dx.doi.org/10.1119/1.16640.

[47] J. Jackle, Models of the glass transition, Rep. Progr. Phys. 49 (2) (1986) 171, http://dx.doi.org/10.1088/0034-4885/49/2/002.

[48] M. Stringe, H. Rösner, G. Wilde, Evidence for strain and a structural reset in $Pd_{40}Ni_{40}P_{20}$ bulk metallic glass, J. Appl. Phys. 132 (10) (2022) 105107, http://dx.doi.org/10.1063/5.0098050.

[49] N. Sohrabi, J.E.K. Schawe, J. Jhabvala, J.F. Löffler, R.E. Logé, Critical crystallization properties of an industrial-grade Zr-based metallic glass used in additive manufacturing, Scr. Mater. 199 (2021) 113861, http://dx.doi.org/10.1016/j.scriptamat.2021.113861.

[50] P. Zhang, J.J. Maldonis, M.F. Besser, M.J. Kramer, P.M. Voyles, Medium-range structure and glass forming ability in Zr–Cu–Al bulk metallic glasses, Acta Mater. 109 (2016) 103–114, http://dx.doi.org/10.1016/j.actamat.2016.02.006.

[51] J. Hwang, Z.H. Melgarejo, Y.E. Kalay, I. Kalay, M.J. Kramer, D.S. Stone, P.M. Voyles, Nanoscale structure and structural relaxation in $Zr_{50}Cu_{45}Al_5$ bulk metallic glass, Phys. Rev. Lett. 108 (2012) 195505, http://dx.doi.org/10.1103/PhysRevLett.108.195505.

[52] M.W. da Silva Pinto, L. Daum, H. Rösner, G. Wilde, Correlations between shadow glass transition, enthalpy recovery and medium range order in a $Pd_{40}Ni_{40}P_{20}$ bulk metallic glass , Acta Mater. 275 (2024) 120034, http://dx.doi.org/10.1016/j.actamat.2024.120034.

[53] A. Hassanpour, S. Hilke, H. Rösner, S.V. Divinski, G. Wilde, Impact of severe plastic deformation on the relaxation of glassy and supercooled liquid states of amorphous $Pd_{40}Ni_{40}P_{20}$, J. Appl. Phys. 128 (2020) 155107, http://dx.doi.org/10.1063/5.0026950.

[54] S. Wei, M. Stolpe, O. Gross, Z. Evenson, I. Gallino, W. Hembree, J. Bednarcik, J.J. Kruzic, R. Busch, Linking structure to fragility in bulk metallic glass-forming liquids, Appl. Phys. Lett. 106 (2015) 181901, http://dx.doi.org/10.1063/1.4919590.

[55] D.B. Williams, C.B. Carter, Transmission Electron Microscopy, second ed., Springer New York, NY, 2009, http://dx.doi.org/10.1007/978-0-387-76501-3.

[56] Z. Evenson, B. Ruta, S. Hechler, M. Stolpe, E. Pineda, I. Gallino, R. Busch, X-ray photon correlation spectroscopy reveals intermittent aging dynamics in a metallic glass, Phys. Rev. Lett. 115 (17) (2015) 175701, http://dx.doi.org/10.1103/PhysRevLett.115.175701.

[57] A. Das, P.M. Derlet, C. Liu, E.M. Dufresne, R. Maaß, Stress breaks universal aging behavior in a metallic glass, Nat. Commun. 10 (2019) 9, http://dx.doi.org/10.1038/s41467-019-12892-1.

[58] A. Das, E.M. Dufresne, R. Maaß, Structural dynamics and rejuvenation during cryogenic cycling in a Zr-based metallic glass, Acta Mater. 196 (2020) 723–732, http://dx.doi.org/10.1016/j.actamat.2020.06.063.

[59] S. Haung, P.M. Voyles, Momentum transfer resolved electron correlation microscopy, Ultramicroscopy 256 (2024) 113886, http://dx.doi.org/10.1016/j.ultramic.2023.113886.

[60] J.C. Qiao, J.M. Pelletier, H.C. Kou, X. Zhou, Modification of atomic mobility in a Ti-based bulk metallic glass by plastic deformation or thermal annealing, Intermetallics 28 (2012) 128–137, http://dx.doi.org/10.1016/j.intermet.2012.04.004.

[61] K. Nakazawa, K. Mitsuishi, K. Iakoubovskii, S. Kohara, K. Tsuchiya, Structure-dynamics relation in metallic glass revealed by 5-dimensional scanning transmission electron microscopy, NPG Asia Mater. 16 (2024) 06521, http://dx.doi.org/10.1038/s41427-024-00577-1.